

Time dependent response of thixotropic systems: Insights from small amplitude oscillatory shear

Cite as: Phys. Fluids **32**, 013109 (2020); <https://doi.org/10.1063/1.5134723>

Submitted: 03 November 2019 . Accepted: 02 January 2020 . Published Online: 28 January 2020

Koduvayur A. Ramya , Ramanathan Srinivasan , and Abhijit P. Deshpande 



View Online



Export Citation



CrossMark

ARTICLES YOU MAY BE INTERESTED IN

[A review of thixotropy and its rheological modeling](#)

Journal of Rheology **63**, 477 (2019); <https://doi.org/10.1122/1.5055031>

[Capillary breakup and extensional rheology response of food thickener cellulose gum \(NaCMC\) in salt-free and excess salt solutions](#)

Physics of Fluids **32**, 012113 (2020); <https://doi.org/10.1063/1.5128254>

[Effect of couple stresses on the rheology and dynamics of linear Maxwell viscoelastic fluids](#)

Physics of Fluids **32**, 013108 (2020); <https://doi.org/10.1063/1.5140568>

Scilight Highlights of the best new research
in the physical sciences

LEARN MORE



Time dependent response of thixotropic systems: Insights from small amplitude oscillatory shear

Cite as: Phys. Fluids 32, 013109 (2020); doi: 10.1063/1.5134723

Submitted: 3 November 2019 • Accepted: 2 January 2020 •

Published Online: 28 January 2020



Koduvayur A. Ramya,  Ramanathan Srinivasan,  and Abhijit P. Deshpande^{a)} 

AFFILIATIONS

Department of Chemical Engineering, Indian Institute of Technology Madras, Chennai 600036, India

^{a)} Author to whom correspondence should be addressed: abhijit@iitm.ac.in

ABSTRACT

Thixotropic materials belong to the important class of time dependent, evolving, and aging systems. Their characteristics are currently understood through rheological measurements of steady and step shear wherein the steady states reached at large deformations and the transition from one steady state to another are monitored. Small deformation protocols are not well explored for such systems. This is contrary to the common approach of probing equilibrium state and small perturbations from the equilibrium state initially by focusing on linear viscoelasticity. This work addresses the question of how to understand thixotropic materials by focusing on both the small and large deformations. A model suspension of fumed silica in polyisobutylene/paraffin oil is characterized using steady shear, transient shear, and oscillatory shear rheology. The physical processes occurring due to structural changes during each of the tests are interpreted from the corresponding response. Several structural kinetics and elastoplastic/viscoelastic phenomenological models are evaluated, and a novel combination of models is proposed to obtain the description of the responses to various tests. The advantage of this strategy is highlighted in terms of possible difference in the mechanisms at small and large deformations. Kramers–Kronig relations are used to examine the experimental and simulated dataset obtained from oscillatory shear to identify possible violation of linearity or time independence. We demonstrate that the analysis of the oscillatory response using Kramers–Kronig relations leads to important insights about these systems.

Published under license by AIP Publishing. <https://doi.org/10.1063/1.5134723>

I. INTRODUCTION

Structured materials exhibit rich and diverse rheological behavior, encompassing varied response time scales.^{1–4} Interestingly, material systems with weakly aggregated structures are known to display reversible time-dependent changes in viscosity during and after deformation, a phenomenon that is often defined as thixotropy.^{5–9} It is postulated that in these materials, flow-induced structural events occur, viz., the aggregated flocs that form a space-filling network structure deform and breakdown leading to shear thinning.^{8,10,11} In some cases, shear induced flocculation occurs due to hydrodynamic and particle interactions leading to shear thickening.^{12,13} When the deformation rate decreases or ceases, a structure builds up due to Brownian motion.^{14,15} Since a particulate network has the ability to store energy and release the same beyond a critical stress, most thixotropic systems also simultaneously exhibit viscoelasticity and plasticity.^{10,16–19} Hence, although an equilibrium state (when no shear is applied) and a steady state (under a given shear) may exist in these systems, the approach

to the steady/equilibrium state can be slow/fast depending on the time scales of rheological measurements.^{8,9,17,19,20} Therefore, experimental and theoretical probing of the thixotropic elastoviscoplastic (TEVP) behavior is challenging and is of utmost interest among rheologists^{8–10,21–24} and among the larger community studying aging non-equilibrium systems.^{25–28}

For probing TEVP behavior, a simple and common protocol is to perform step-wise changes in the shear rate ($\dot{\gamma}$) from $\dot{\gamma}_i$ to $\dot{\gamma}_{f,up}$ (i.e., step-up from the initial to final shear rate) or $\dot{\gamma}_i$ to $\dot{\gamma}_{f,down}$ (i.e., step-down). The changes in stress (τ) from τ_i to $\tau_{f,up}$ (during step-up) or τ_i to $\tau_{f,down}$ (during step-down) are monitored, as shown in Fig. 1(a). For a TEVP system, the step tests indicate viscoelastic as well as dominant thixotropic structure breakdown/buildup phenomena. Based on the magnitude of shear rates, a pre-yield/post-yield response can also be identified.^{8,10,20,21,29} Another standard rheological test includes a shear rate ramp wherein the post-yield and thixotropic response of the material are clearly manifested.^{8,9} Of late, several other protocols ranging from transient shear tests (such as triangular ramp, flow reversal, and intermittent

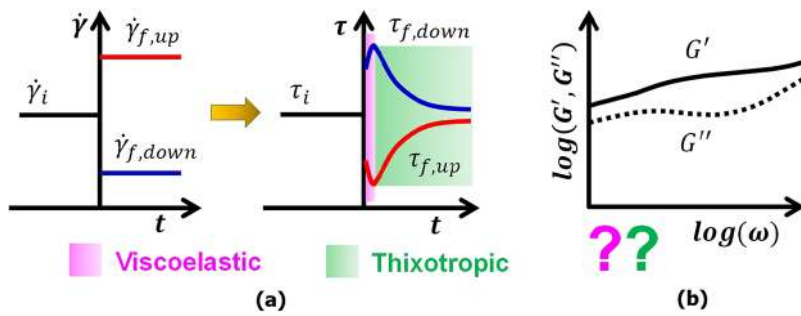


FIG. 1. A schematic representation of (a) step up/step down and (b) frequency sweep (SAOS) response of TEVP systems.

step shear), long time creep/stress relaxation to oscillatory shear, and unidirectional large amplitude oscillatory shear tests are being explored.^{7–10,18,21–24,30–32} Insights from such complex flows are helpful in distinguishing/isolating thixotropy from other rheological phenomena.^{9,10,23,24,27,28} Small amplitude oscillatory shear (SAOS) is a widely used protocol; however, the response of TEVP materials in SAOS does not seem to have any distinct signatures [Fig. 1(b)]. The limits of linear viscoelasticity may not also be clearly defined for such systems.^{21,24} Therefore, SAOS of TEVP systems is not well explored.

In general, material response functions and the inter-relations among them are useful analysis tools. As an example, the Kramers–Kronig (KK) relations can be utilized to obtain useful information and insights from the SAOS response. KK relations are often utilized for the analysis of susceptibilities in linear and non-linear regimes,^{33,34} and in this work, we propose their use in exploring the dominant mechanisms during SAOS and in the modeling of the overall response.

Common thixotropic models differ based on the type of equation for stress tensor.^{8,16,35,36} Certain literature make use of a viscoelastic solid-like equation such as Kelvin–Voigt and Bingham plastic.^{4,20,21,29,31,32,37} Alternatively, viscoelastic liquid-like equations, such as Maxwell and Giesekus, are derived from the conventional rate-type models, and their multimode version is also adopted.^{20,21,30,38–40} The simplest rate-type model is an Oldroyd 8-constant generalized constitutive formulation given by⁴¹

$$\begin{aligned} \boldsymbol{\tau} + \lambda_1 \overset{\nabla}{\boldsymbol{\tau}} + \frac{1}{2} \lambda_3 \{ \dot{\boldsymbol{\gamma}} \cdot \boldsymbol{\tau} + \boldsymbol{\tau} \cdot \dot{\boldsymbol{\gamma}} \} + \frac{1}{2} \lambda_5 (tr \boldsymbol{\tau}) \dot{\boldsymbol{\gamma}} + \frac{1}{2} \lambda_6 (\boldsymbol{\tau} : \dot{\boldsymbol{\gamma}}) \boldsymbol{\delta} \\ = -\eta_0 \left[\dot{\boldsymbol{\gamma}} + \lambda_2 \overset{\nabla}{\dot{\boldsymbol{\gamma}}} + \lambda_4 \{ \dot{\boldsymbol{\gamma}} \cdot \dot{\boldsymbol{\gamma}} \} + \frac{1}{2} \lambda_7 (\dot{\boldsymbol{\gamma}} : \dot{\boldsymbol{\gamma}}) \boldsymbol{\delta} \right], \end{aligned} \quad (1)$$

where $\boldsymbol{\tau}$ is the stress tensor and $\dot{\boldsymbol{\gamma}}$ is the strain rate tensor. The superscript “ ∇ ” represents the upper convected derivative of corresponding quantities. The model includes all possible quadratic terms such as $\dot{\boldsymbol{\gamma}} \cdot \boldsymbol{\tau}$, $\boldsymbol{\tau} \cdot \dot{\boldsymbol{\gamma}}$, $\boldsymbol{\tau} : \dot{\boldsymbol{\gamma}}$, $\dot{\boldsymbol{\gamma}} \cdot \dot{\boldsymbol{\gamma}}$, and $\dot{\boldsymbol{\gamma}} : \dot{\boldsymbol{\gamma}}$. Furthermore, it has 8 parameters, namely, relaxation times, $\lambda_1, \dots, \lambda_7$, and zero-shear rate viscosity, η_0 . It reduces to the Newtonian fluid model when $\lambda_1 = \dots = \lambda_7 = 0$ and to the convected Maxwell model when $\lambda_2 = \dots = \lambda_7 = 0$. Other rate-type models, such as the Giesekus and Phan-Thien–Tanner, are an extension of the Oldroyd 8-constant model with additional nonlinear stress terms. The constitutive equations of Giesekus model are given by⁴¹

$$\boldsymbol{\tau} = \boldsymbol{\tau}_s + \boldsymbol{\tau}_p, \quad (2a)$$

$$\boldsymbol{\tau}_s = -\eta_s \dot{\boldsymbol{\gamma}}, \quad (2b)$$

$$\boldsymbol{\tau}_p + \lambda_1 \overset{\nabla}{\boldsymbol{\tau}}_p - \alpha \frac{\lambda_1}{\eta_p} \{ \boldsymbol{\tau}_p \cdot \boldsymbol{\tau}_p \} = -\eta_p \dot{\boldsymbol{\gamma}}, \quad (2c)$$

where the total stress tensor, $\boldsymbol{\tau}$, is written as a superposition of solvent and polymer contributions, $\boldsymbol{\tau}_s$ and $\boldsymbol{\tau}_p$, respectively [Eq. (2a)]. $\boldsymbol{\tau}_s$ follows a Newtonian fluid model [Eq. (2b)]. The expression for $\boldsymbol{\tau}_p$ is obtained from the convected Maxwell model with the addition of the nonlinear stress term of the form underlined in Eq. (2c). Upon replacing $\boldsymbol{\tau}_p$ in Eq. (2c) with $\boldsymbol{\tau} + \eta_s \dot{\boldsymbol{\gamma}}$ [obtained by substituting Eq. (2b) into (2a)], a single constitutive equation of the following form is obtained:

$$\begin{aligned} \boldsymbol{\tau} + \lambda_1 \overset{\nabla}{\boldsymbol{\tau}} - a \frac{\lambda_1}{\eta_0} \{ \boldsymbol{\tau} \cdot \boldsymbol{\tau} \} - a \lambda_2 \{ \dot{\boldsymbol{\gamma}} \cdot \boldsymbol{\tau} + \boldsymbol{\tau} \cdot \dot{\boldsymbol{\gamma}} \} \\ = -\eta_0 \left[\dot{\boldsymbol{\gamma}} + \lambda_2 \overset{\nabla}{\dot{\boldsymbol{\gamma}}} - a \frac{\lambda_2^2}{\lambda_1} \{ \dot{\boldsymbol{\gamma}} \cdot \dot{\boldsymbol{\gamma}} \} \right], \end{aligned} \quad (2d)$$

$$\eta_0 = \eta_s + \eta_p, \quad \lambda_2 = \lambda_1 \frac{\eta_s}{\eta_p}, \quad a = \frac{\alpha}{1 - (\lambda_2/\lambda_1)}, \quad (2e)$$

where the model parameters, η_s and η_p , are the solvent and polymer contributions to the zero-shear rate viscosity, η_0 , respectively, and λ_1 is the characteristic relaxation time. It can be noted that the Giesekus model [Eqs. (2d) and (2e)] is similar to the Oldroyd model [Eq. (1)] except for the additional nonlinear stress term and $\lambda_3 = -2a\lambda_2$, $\lambda_4 = -a\frac{\lambda_2^2}{\lambda_1}$, and $\lambda_5 = \lambda_6 = \lambda_7 = 0$. The dimensionless mobility factor, α , has been attributed to the anisotropy of Brownian motion and/or hydrodynamic drag on the constituent polymer molecule. Apart from the viscoelastic solid-like or liquid-like based model, a phenomenological structure evolution equation is also required to capture structural evolution using a scalar parameter, β ($\beta = 0$, fully broken down and $\beta = 1$, fully built up).^{4,16,18,21,29–32,35–37,39,40,42} In some models, fluidity is used as the structure factor, which is inversely related to the structure size or strength.^{17,21,42} The structure factor is either empirically related to rheological properties (such as viscosity and yield stress)^{4,16,18,21,29–32,35–37,39,40,42} or based on specific microstructural physical insights.^{7,43,44} Recently, several models have been developed and are shown to satisfactorily capture many aspects of the TEVP behavior in steady and transient shear test protocols.^{9,10,22–24,45,46} Although the models include additional features such as multiple thixotropic relaxation time scales and evolution of yield stress, they render an unsatisfactory description for SAOS probably due to insufficient incorporation of viscoelasticity. In addition, the structural response at low deformations may be fundamentally very different compared to that at large deformations, within a cycle. Therefore, it is necessary to explicate relevant

structural mechanisms and include the corresponding response features in the models.

In this work, a comparative study of SAOS response of a model TEVP suspension of fumed silica in polyisobutylene/paraffin oil (FS-PIB-PO) with that of the pure suspending medium, polyisobutylene/paraffin oil (PIB-PO), and pure particle suspension (FS-PO) is presented to comprehend the corresponding rheological phenomena such as viscoelasticity, plasticity, and thixotropy. KK analysis is performed on the SAOS experimental data to complement the understanding. Steady and transient shear tests are also carried out to illustrate that they are necessary in combination with SAOS to understand the structural characteristics of TEVP systems. Based on the insights, different structure kinetics-based models are evaluated. SAOS results show that the structure is more complex than what is usually interpreted from steady and step shear tests. Therefore, suitable modifications are suggested to get a more complete model, which can accurately capture the response of the test protocols including SAOS. Using KK analysis, the effect of thixotropic parameters on the SAOS model predictions is highlighted.

II. EXPERIMENTAL METHODS

A. Materials and sample preparation

The material system studied in our work is a model thixotropic suspension prepared by closely following the protocol mentioned in the literature.⁴⁷ The suspension consists of 2.9 vol. % hydrophobic fumed silica (Evonik, Aerosil® R972) in a blend of 69 wt. % paraffin oil (Merck, density: 0.827–0.890 g/cc) and 31 wt. % polyisobutylene (PIB) (BASF, Glissopal® 1000, density at 20 °C: 0.89 g/cc). Although the primary particles in fumed silica have a nominal radius of 16 nm, it is known that they rarely remain in isolation and usually aggregate into micrometer sized agglomerates.^{21,47} The suspending medium was first prepared by mixing PIB in paraffin oil at a high temperature of 100 °C in a beaker (on an oil bath) under magnetic stirring of 1000 rpm. The blend system, thus, obtained was designated as PIB-PO. The fumed silica aggregates were then dispersed in the blend by mixing in a homogenizer at 8000 rpm for 30 min followed by magnetic stirring at 1000 rpm for 2 h. This was followed by heating the sample in a vacuum oven at 60 °C until all the air bubbles disappeared. The sample was then stored for slow aging up to 3 weeks. The model suspension, thus, obtained was designated as FS-PIB-PO. A similar procedure was followed for the preparation of fumed silica (2.9 vol. %) in paraffin oil (69 wt. %) suspension designated as FS-PO. Standard silicone oils with constant viscosities designated by Brookfield® and Wacker® were used as procured.

B. Rheological measurements

The tests were performed in the strain rate controlled mode using an Anton Paar MCR 301 rheometer with a cone and plate geometry of 25 mm diameter, 1° angle of inclination, and 52 μm truncation gap. The sample from an aged batch is loaded on to the Peltier at 25 °C temperature. All the steady and transient shear tests were preceded by a pre-shear of 300 s⁻¹ for 300 s to obtain a nearly broken down initial structure. On the other hand, SAOS

results reported here are for the non-pre-sheared initial state. Data were collected using the rheometer software “Rheoplus”. All the tests were performed thrice to ensure repeatability. A few experiments were also conducted with a twin-drive (separate motor) MCR 702 rheometer in the strain controlled mode, and these results were in good agreement with the results obtained from MCR 301. Furthermore, it was ensured that only the results obtained for shear rates that were achieved as commanded are reported and used for modeling.

The samples were subjected to step-wise changes in shear rate ($\dot{\gamma}$) to monitor the changes in corresponding stresses (τ) as a function of time. Step up shear tests were performed from $\dot{\gamma}_{i,up} = 0.1 \text{ s}^{-1}$ to $\dot{\gamma}_{f,up} = 0.25 \text{ s}^{-1}, 0.5 \text{ s}^{-1}, 2.5 \text{ s}^{-1},$ and 5 s^{-1} , respectively. Similarly, step down shear tests were performed from $\dot{\gamma}_{i,down} = 5 \text{ s}^{-1}$ to $\dot{\gamma}_{f,down} = 1 \text{ s}^{-1}, 0.5 \text{ s}^{-1}, 0.1 \text{ s}^{-1},$ and 0.05 s^{-1} , respectively. Shear rate sweeps were performed on the samples by varying the shear rates logarithmically from 0.01 s^{-1} to 1000 s^{-1} to obtain the corresponding steady state stresses. For the oscillatory shear measurements, the samples were first subjected to a sinusoidal strain with the amplitude of strain varying logarithmically from 0.1% to 1000% at frequencies of 1 rad s^{-1} and 10 rad s^{-1} , respectively, to determine the critical strain amplitude. For every input strain amplitude, the raw values of 256 data points were recorded in each cycle. Small strain amplitudes are chosen within the critical strain amplitude to further probe the samples in the frequency range of 0.01 rad s^{-1} – 100 rad s^{-1} . The transient shear test of the triangular ramp was performed for a duration of $t_{total} = 72 \text{ s}$ such that the maximum shear rate is achieved at the half time ($\frac{t_{total}}{2}$). The value of the rate of increase/decrease in shear rate was chosen as $slope = 0.05237 \text{ s}^{-2}$ similar to the protocol mentioned elsewhere.^{24,31} In the transient shear test of flow reversal, a constant shear rate was applied initially, until the corresponding steady state stress is achieved. This was followed by a rapid reversal in the direction of shear to negative of the same value of shear rate to obtain the corresponding steady state stress. The shear rates for which flow reversal tests were performed are $-\dot{\gamma}_{of} = \dot{\gamma}_{of} = 0.01 \text{ s}^{-1}, 0.1 \text{ s}^{-1}, 1 \text{ s}^{-1},$ and 10 s^{-1} , respectively.

C. Kramers-Kronig analysis

For a system that is causal, linear, and time independent, the Kramers-Kronig (KK) equations relate the real part (X') and imaginary part (X'') of any complex susceptibility (X^*) arising from it such that the former can be reconstructed from the latter and vice versa. They are given by

$$X'(\omega) = X'(\infty) + \frac{2}{\pi} \int_0^{\infty} \frac{uX''(u) - \omega X''(\omega)}{u^2 - \omega^2} du, \quad (3a)$$

$$X''(\omega) = \frac{2\omega}{\pi} \int_0^{\infty} \frac{X'(u) - X'(\omega)}{u^2 - \omega^2} du, \quad (3b)$$

where ω is the angular frequency of probing. They are widely used in electrical, optical, and electrochemical response.^{11,26,34,48} Validation of electrochemical impedance spectroscopic data is commonly carried out using KK relations.⁴⁸ In rheology, KK relations have been used for dynamic moduli, assuming the response to be linear,^{49–51} and in some instances for validating the data.^{52–54} Some of the challenges in employing KK relations for data validation are the requirement of data in a wide range of frequencies at frequent intervals

and integration over the same. Often, data at high and low frequencies are not available due to equipment limitations and constraints on the duration of experiments.^{51,52,55} Approximated expressions for the KK relations obtained based on plausible assumptions about the response, in some cases, also have their restrictions.^{49,50,53}

An alternate method for KK validation is the measurement model approach wherein the data can be fit to the equivalent circuit of an inherently causal, linear, and time independent model.^{56,57} In this work, we have used a multimode Kelvin–Voigt circuit (Fig. 2) with the circuit elements representing each mode. Since each circuit element in Fig. 2 is KK compliant, the entire circuit is KK compliant and so will be the data that can be perfectly fit. An easy-to-use software application called “Linear KKT,” implementing this approach and made freely available online, had been utilized to analyze impedance data in the literature.^{56,57} If the total number of experimental frequencies (ω) is N , the method introduces M elements in the circuit with associated time constants (λ_{KK}) such that they are logarithmically spaced over the inverse ω range with $\lambda_{KK-1} = \omega_1^{-1}$ and $\lambda_{KK-M} = \omega_N^{-1}$ (always $M < N$). Then, the complex modulus of the corresponding model is given by

$$G_{KK}^*(\omega_i) = G_\infty + \sum_{k=1}^M G_k \left[\frac{1}{1 + \omega_i^2 \lambda_{KK-k}^2} - j \frac{\omega_i \lambda_{KK-k}}{1 + \omega_i^2 \lambda_{KK-k}^2} \right], \quad (4)$$

where $i \in 1, \dots, N$ and $k \in 1, \dots, M$. In order to verify whether the data can be modeled adequately or not, by the chosen circuit, the differences between experimental and model values, referred to as “residuals,” are calculated as

$$\Delta'(\omega_i) = \frac{G'_{\text{experimental}}(\omega_i) - G'_{KK}(\omega_i)}{|G_{KK}^*(\omega_i)|} \times 100, \quad (5a)$$

$$\Delta''(\omega_i) = \frac{G''_{\text{experimental}}(\omega_i) - G''_{KK}(\omega_i)}{|G_{KK}^*(\omega_i)|} \times 100. \quad (5b)$$

The number of circuits (i.e., the value of M) is increased until no further decrease in the residuals is observed. The residuals, thus, obtained are examined for their magnitude and trends. If the residuals are small and randomly distributed, the data are considered to be KK compliant. If the residuals are large and exhibit any systematic trend with frequency, the data are not KK compliant. Such deviations from KK compliance indicate non-causal, nonlinear, and/or time dependent response. An advantage of this method is that the validation can be performed even if the data are available in a limited frequency range.

Earlier, Mours and Winter performed time-resolved rheometry to analyze a partially crosslinked polycarbonate system that exhibits time varying phenomena due to thermally induced changes. They defined a dimensionless quantity called mutation number, N_{mu} , as

the ratio of experimental (or observation) time, t_{expt} , to that of the mutation time, t_{mu} , of a structurally evolving material. t_{mu} is the time required for a $(1/e)$ -change in the property “ X ” of a material at an instantaneous rate of change in its value, i.e., dX/dt .⁵⁸ If t_{expt} is much less than t_{mu} , the material property appears constant. If t_{expt} is greater than t_{mu} , then the time change of the material property, i.e., thermally induced changes, can be identified. Hence, when N_{mu} is large, the material response is time dependent, and when it is small, the response can be considered as time independent. This analysis is, in principle, similar to oscillatory tests and thixotropic response. Depending on the thixotropic time scales, we can have two responses: (1) the oscillatory response is “linear response” of the material with equilibrium structure and (2) the oscillatory response is indicative of thixotropic structural changes in the material. The KK analysis, on its own, cannot be used to identify which of the three conditions (i.e., causality, linearity, and time independence) are violated. However, it is important to note that in the context of our work, the KK residuals would carry the similar information as that of N_{mu} . Therefore, large KK residuals imply time dependent phenomena, since linearity and causality conditions are satisfied. In this work, the oscillatory shear response is due to the time dependent structural evolution of thixotropic materials. Hence, the oscillatory shear response of various experimental data and model results was analyzed using linear KKT. The fit, and therefore departure from KK compliance, was quantified using the residuals calculated from Eq. (5). This procedure is referred to as “KK analysis”.

D. Parameter optimization

Several models were evaluated and are discussed in Sec. III D. The model equations and the corresponding optimized parameters are presented in Table I and Tables S2–S4 of the supplementary material. A constrained optimization algorithm, specifically “fmincon” in MATLAB®, was employed to obtain these best fit model parameters. The relative difference between the model predicted and experimental SAOS data (of moduli) was minimized with a constraint that the predicted steady shear, step up and step down shear data (of stresses) were within a small percent (~ 2.5) of the corresponding experimental data. The SAOS, steady shear, and 4 sets each of step up and step down shear were used in the optimization. Based on the relative error, thus obtained for each of these tests, the effectiveness of the corresponding model predictions is decided. The criteria used to delineate good (***) , moderate (**), and poor (*) match of model predictions with experimental results were chosen as <20 , <40 (i.e., twice the error compared to “***”), and >40 , respectively, for SAOS, <5 , <10 , and >10 , respectively, for steady and step shear tests. The combined model proposed in this work was able to fit the SAOS data with the

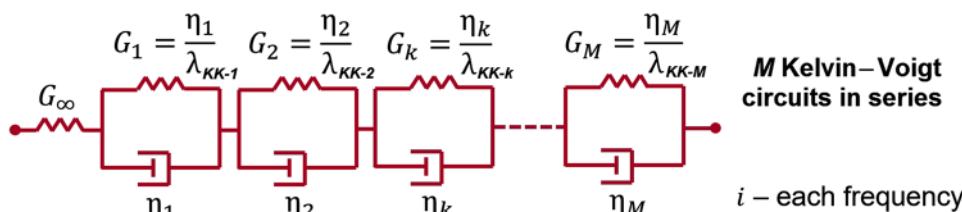


FIG. 2. A schematic representation of the multimode Kelvin–Voigt circuit to fit SAOS data.

TABLE I. Set of equations of the proposed combined Giesekus with structure kinetics and SST model.

Giesekus with structure kinetics submodel	$\tau_G + \lambda_1 \dot{\tau}_G - a \frac{\lambda_1}{\eta_0} \{ \tau_G \cdot \tau_G \} - a \lambda_2 \{ \dot{\gamma} \cdot \tau_G + \tau_G \cdot \dot{\gamma} \} = -\eta_0 \left[\dot{\gamma} + \lambda_2 \dot{\gamma} - a \frac{\lambda_2}{\lambda_1} \{ \dot{\gamma} \cdot \dot{\gamma} \} \right]$ $\frac{d\beta_G}{dt} = k_{Brown-G} [-t_{r1-G} \beta_G \dot{\gamma} + (1 - \beta_G)]$ $\lambda_1 = \lambda_{10} \beta_G; \eta_p = \eta_{p0} \beta_G$ $\eta_0 = \eta_s + \eta_p; \lambda_2 = \lambda_1 \frac{\eta_s}{\eta_p}; a = \frac{\alpha}{1 - (\lambda_2/\lambda_1)}$
SST submodel	$\tau_S = \tau_y + \eta \dot{\gamma} + \eta_\infty \dot{\gamma}$ $\frac{d\beta_S}{dt} = k_{Brown-S} [-t_{r1-S} \beta_S \dot{\gamma} + (1 - \beta_S)]$ $\tau_y = \beta_S \tau_{y0}; \eta = \beta_S \eta_{ST}$
Combined model	$\tau = W_G \tau_G + W_S \tau_S; W_G + W_S = 1$

aforementioned constraints. The corresponding optimized parameters were used for further prediction of the flow reversal and triangular ramp tests (i.e., these experimental data were not used in the optimization).

III. RESULTS AND DISCUSSION

In this section, we first describe the oscillatory shear response of polyisobutylene in a paraffin oil (PIB-PO) blend system, fumed silica in paraffin oil (FS-PO), and fumed silica in polyisobutylene/paraffin oil (FS-PIB-PO) suspensions. The SAOS results are presented in combination with KK analysis. We then compare the stresses obtained from SAOS with those of steady shear for the PIB-PO and FS-PIB-PO to understand the corresponding structural response. Similarly, we also highlight the TEVP behavior of

FS-PIB-PO as obtained from steady shear and transient shear tests such as step shear, triangular ramp, and flow reversal. Based on the results, various models are evaluated and an appropriate model is formulated to capture the TEVP behavior. The characteristics of SAOS response of the models are then discussed along with KK analysis.

A. Oscillatory shear and KK analysis

The oscillatory shear response and corresponding KK analysis of the polyisobutylene/paraffin oil blend system, PIB-PO, is shown in Fig. 3. The strain amplitude sweep (at frequencies of 1 rad s⁻¹ and 10 rad s⁻¹) of PIB-PO indicates a Newtonian fluid-like response, i.e., a dominant constant loss modulus (G'') throughout as shown in Fig. 3(a). The values of storage modulus (G') are not reported as they were low and noisy. In addition, the moduli corresponding to

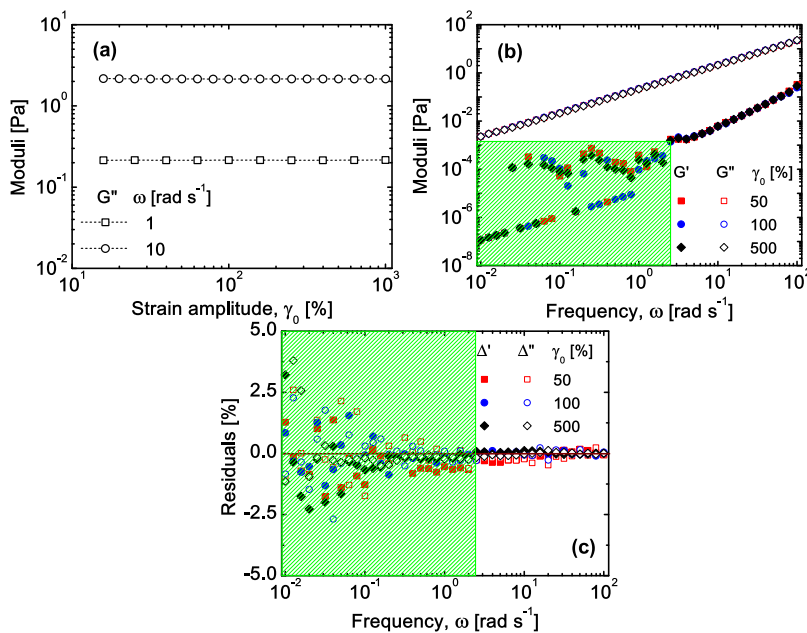


FIG. 3. Polyisobutylene/paraffin oil blend system, PIB-PO. (a) Strain amplitude sweep at frequencies of 1 rad s⁻¹ and 10 rad s⁻¹. (b) Frequency sweep at strain amplitudes of 50%, 100%, and 500%. (c) Residuals from the KK analysis of data shown in (b) computed using Eq. (5).

strain amplitudes below 15% are omitted as their torque values were close to the equipment sensitivity. Therefore, strain amplitudes of 50%, 100%, and 500% were chosen for the frequency sweep measurements. It can be seen from Fig. 3(b) that at all frequencies and strain amplitudes, G' is lower than G'' by more than an order of magnitude. G'' values also exhibit a frequency dependence with an approximate slope of 1. Although G' values are low and noisy below 2.5 rad s^{-1} frequency [shaded region in Fig. 3(b)], they exhibit a frequency dependence with an approximate slope of 2 throughout, indicating a purely viscous behavior. This is expected given the low molecular weight/concentration of the polymer, due to which the effects such as chain elasticity, orientation, and entanglement are absent. KK circuit fits are performed on the data, and the corresponding residuals are computed using Eq. (5) and presented in Fig. 3(c). The residuals are slightly high at low frequencies [shaded region in Fig. 3(c)], which is due to the noisy G' values at low frequencies. Overall, the residuals are low and randomly distributed, confirming that the data are KK compliant. This indicates that the SAOS response satisfies causality, linearity, and time independence conditions.

The oscillatory shear response and the corresponding KK analysis of the fumed silica in paraffin oil suspension, FS-PO, is shown in Fig. 4. The strain amplitude sweep (at frequencies of 1 rad s^{-1} and 10 rad s^{-1}) of FS-PO indicates a crossover from $G' > G''$ to $G'' > G'$ along with a slight peak in G'' beyond a critical strain amplitude of 1%, as shown in Fig. 4(a). Therefore, strain amplitudes of 0.25%, 0.5%, and 1% were chosen for the frequency sweep measurements. It is seen from Fig. 4(b) that at these strain amplitudes, both the moduli exhibit a weak frequency dependence, with $G' > G''$ throughout the frequency range studied, by half an order of magnitude. Given the hydrophilic surface silanol groups on the majorly hydrophobic fumed silica, their flocculation in paraffin oil (weakly H-bonding, non-polar solvent) is expected.^{59,60} The oscillatory shear response

also suggests a network structure of the flocs. An increase in G'' (at all frequencies) is observed with an increase in strain amplitude, leading to an increase in the damping factor, $\tan(\delta)$ ($=G''/G'$). This indicates a more enhanced disruption of the weak flocculated structure, leading to an increased dissipation. This is commonly referred to as a change in the extent of structural breakdown. This phenomenon manifests as an increase in the residuals, $|\Delta'|$ and $|\Delta''|$ (at all frequencies), with strain amplitude in the corresponding KK analysis plots shown in Fig. 4(c). Given that the magnitude of residuals are high and they exhibit a definitive trend, it is clear that the data are not KK compliant. This indicates that the corresponding response violates one or more of the three conditions, viz., causality, linearity, and time independence, e.g., inherent time dependence exhibited by thixotropic fluids.

The oscillatory shear response and the corresponding KK analysis of the fumed silica in polyisobutylene/paraffin oil suspension, FS-PIB-PO, is shown in Fig. 5. It should be noted that this is an extremely popular model experimental system for investigating thixotropy.^{10,20–22,47} The strain amplitude sweep (at frequencies of 1 rad s^{-1} and 10 rad s^{-1}) of FS-PIB-PO, shown in Fig. 5(a), indicates a response similar to that of the pure particle suspension, FS-PO [Fig. 4(a)], except that the FS-PIB-PO system exhibits a stronger peak in G'' around the critical strain amplitude of 1%. At small strain amplitudes of 0.25%, 0.5%, and 1%, a weak frequency dependence with viscoelastic solid-like response is prevalent as shown in Fig. 5(b). Furthermore, a slight decrease in G'' as well as a greater decrease in G' (at all frequencies) with an increase in strain amplitude is evident. The greater decrease in G' suggests disruption of the PIB mediated network structure, in addition to the disruption of flocculated structure. This leads to a slight increase in $\tan(\delta)$, which is reflected only as minimal changes in $|\Delta'|$ and $|\Delta''|$ (at all frequencies) with an increase in strain amplitude in the corresponding KK analysis plots shown in Fig. 5(c). These results suggest that fumed

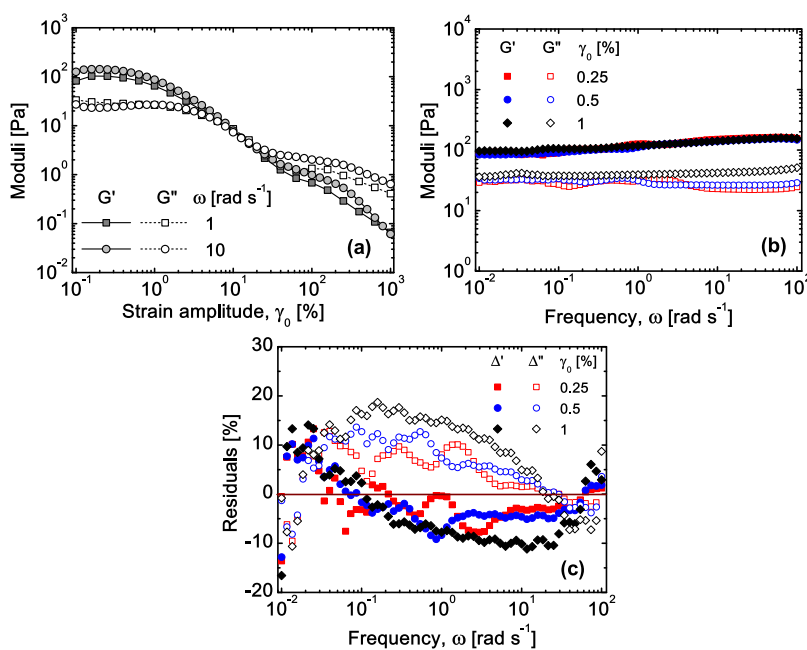


FIG. 4. Fumed silica in paraffin oil suspension, FS-PO. (a) Strain amplitude sweep at frequencies of 1 rad s^{-1} and 10 rad s^{-1} . (b) Frequency sweep at strain amplitudes of 0.25%, 0.5%, and 1%. (c) Residuals from the KK analysis of data shown in (b) computed using Eq. (5).

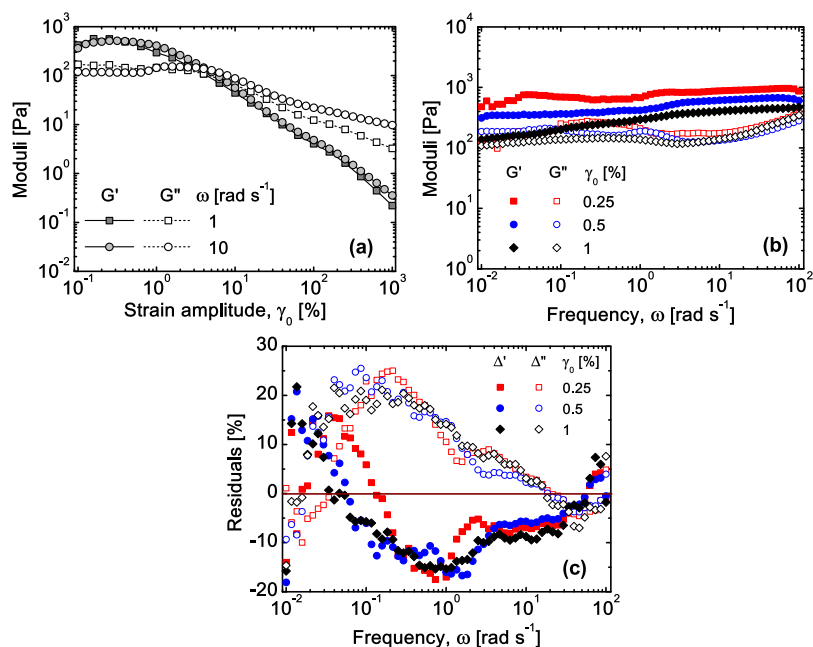


FIG. 5. Fumed silica in polyisobutylene/paraffin oil suspension, FS-PIB-PO. (a) Strain amplitude sweep at frequencies of 1 rad s⁻¹ and 10 rad s⁻¹. (b) Frequency sweep at strain amplitudes of 0.25%, 0.5%, and 1%. (c) Residuals from the KK analysis of data shown in (b) computed using Eq. (5).

silica particles flocculate in the PIB-PO mixture as well to form a weak network structure. However, the ability of particles to flocculate is greatly affected by the tendency of PIB chains to adsorb on their surface and reduce the inter-particle interactions. It is known that the thixotropic time scales are slowed down in such cases than that of a pure particle suspension.⁴⁷ This could be the reason for higher magnitudes of residuals of moduli in the case of FS-PIB-PO as shown in Fig. 5(c) than that of FS-PO as shown in Fig. 4(c). Furthermore, these residuals exhibit a definitive trend, confirming that the data are not KK compliant, and this is along the expected lines.

KK analysis was also performed on standard fluids (refer to Figs. S1–S3 and Table S1 of the supplementary material). As expected, the SAOS of standard fluids exhibit good KK compliance, indicating that the conditions of causality, linearity, and time independence are not violated. Thus, it is clear that KK analysis of SAOS data is sensitive to violations of the linearity, causality, and time independence conditions.

B. Comparison of SAOS and steady shear

The response of steady shear rate ramp test, which is usually used for characterizing non-linear rheology, is shown in Figs. 6(a) and 6(b) for the PIB-PO blend system and FS-PIB-PO suspension, respectively. The stresses during their frequency sweeps [shown in Figs. 3(b) and 5(b)] are also plotted against the corresponding shear rates ($\dot{\gamma}_0 = \gamma_0 \omega$) in Figs. 6(a) and 6(b). It is seen from Fig. 6(a) that PIB-PO exhibits a proportional increase in the stress with shear rate during steady shear as well as frequency sweep, and the results from steady shear and frequency sweep practically overlap, confirming a simple structure and Newtonian fluid behavior. For the FS-PIB-PO suspension during steady shear [Fig. 6(b)], the stresses exhibit a less-pronounced increase, i.e., shear thinning ($\sim 10^{-2} - 10^0$ s⁻¹) followed by an increase with the shear rate (post 10⁰ s⁻¹). However, during frequency sweep, the stresses only slightly increase with the shear rate with the increase being stronger at the higher strain amplitude of 1%. This mismatch in the steady shear and SAOS response of

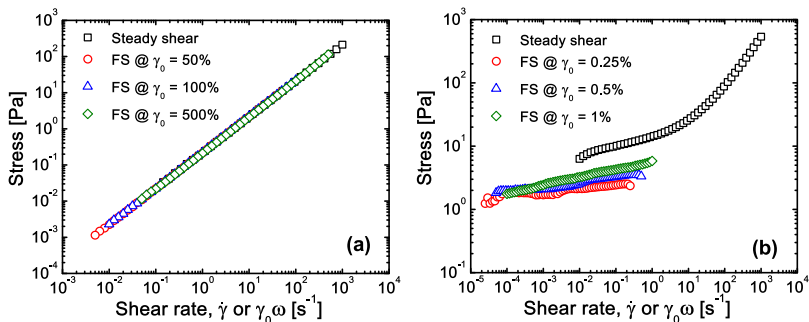


FIG. 6. Stress as a function of shear rate during steady shear and frequency sweep of (a) the PIB-PO blend system (at strain amplitudes of 50%, 100%, and 500%) and (b) the FS-PIB-PO suspension (at strain amplitudes of 0.25%, 0.5%, and 1%).

FS-PIB-PO suspension clearly indicates the existence of a complex structure. It is also important to note that the low shear rates that were not achieved during steady shear can also be probed by SAOS. Thus, the processes, which strongly affect the result, could be different for SAOS and steady shear tests. Most models in the literature provide good predictions of the response during large deformation protocols but do an unsatisfactory modeling of SAOS for such TEVP systems as these models miss this aspect of the material behavior (refer Sec. II 2 of the [supplementary material](#)).

C. Transient shear

The response of the step up and step down shear tests for FS-PIB-PO suspension is presented in Figs. 7(a) and 7(b), respectively. Such data had also been reported by several others earlier.^{10,20–22} It can be seen that there is an initial fast viscoelastic rise/decay in stress followed by a gradual decrease/increase to steady state representing the slow thixotropic time scales contributed by structure breakdown/buildup in step up/step down tests. The viscoelasticity at initial times is prominent especially at lower shear rates of 0.25 s⁻¹, 0.5 s⁻¹ and 0.05 s⁻¹, 0.1 s⁻¹ in step up and step down tests, respectively. However, at higher shear rates of 2.5 s⁻¹, 5 s⁻¹, and 0.5 s⁻¹, 1 s⁻¹ in step up and step down tests, respectively, the response is predominantly thixotropic. This indicates that the break down/rebuilding of the suspension structure post the step change in step up/step down shear tests is slow enough at lower shear rates that the residual elasticity of the structure from the previous history becomes apparent. Figure 7(c) presents the triangular ramp transient shear rate test results for the FS-PIB-PO suspension. It shows that the output stress trajectories during ramp-up in shear rate [$\dot{\gamma} = slope \times (t)$ for $t \leq \frac{t_{total}}{2}$] and ramp-down in shear rate [$\dot{\gamma} = slope \times (t_{total} - t)$ for $t > \frac{t_{total}}{2}$] are slightly different. This asymmetric response indicates hysteresis. As per the protocol, the

maximum input shear rate achieved during the test is 1.89 s⁻¹, which is small enough for some structure to be present but not too low that only elastic contributions are prevalent. Therefore, the corresponding output stress response can be attributed to thixotropy. Similarly, the results of the flow reversal tests for FS-PIB-PO suspension are presented in Fig. 7(d). It can be observed that at low final shear rates, i.e., $\dot{\gamma}_{of} = 0.01 \text{ s}^{-1}$ and 0.1 s^{-1} , there is a two-step increase in stress, leading to a steady state that diminishes to a single-step increase at final shear rates, $\dot{\gamma}_{of} > 0.1 \text{ s}^{-1}$. Usually, the initial stress increase is attributed to viscoelastic relaxation that is predominant at low shear rates and diminishes when shear rates become larger. The second stress increase has been attributed to plastic evolution due to kinematic hardening.^{9,10,24,45,46,61} It was proposed that in the case of TEVP systems, the yield surface shifts in the direction of current shear rate (here, $\dot{\gamma}_{of}$) leading to an increase in yield stress in this direction, with a consequent decrease in the opposite direction, i.e., direction of the past shear rate (here, $-\dot{\gamma}_{oi}$).^{9,10,61} Therefore, it is essential to ensure that viscoelasticity, yielding, and thixotropy are effectively introduced in the model so that the complex response of FS-PIB-PO suspension can be predicted well.

D. Modeling TEVP behavior

The SAOS response of FS-PIB-PO suspension, as described earlier in Sec. III A, indicates the existence of a transient particulate network structure. Viscoelastic fluid-like models such as Maxwell or Giesekus (introduced in Sec. I) incorporate physical mechanisms of polymer solutions such as stretching, orientation, and chain interaction effects similar to network dynamics. They have also been widely used to analyze the response of material systems belonging to the same class (i.e., have network structures) such as micellar solutions and polymeric gels.^{62,63} Hence, they can be utilized as suitable base models to evaluate the response of FS-PIB-PO suspension.

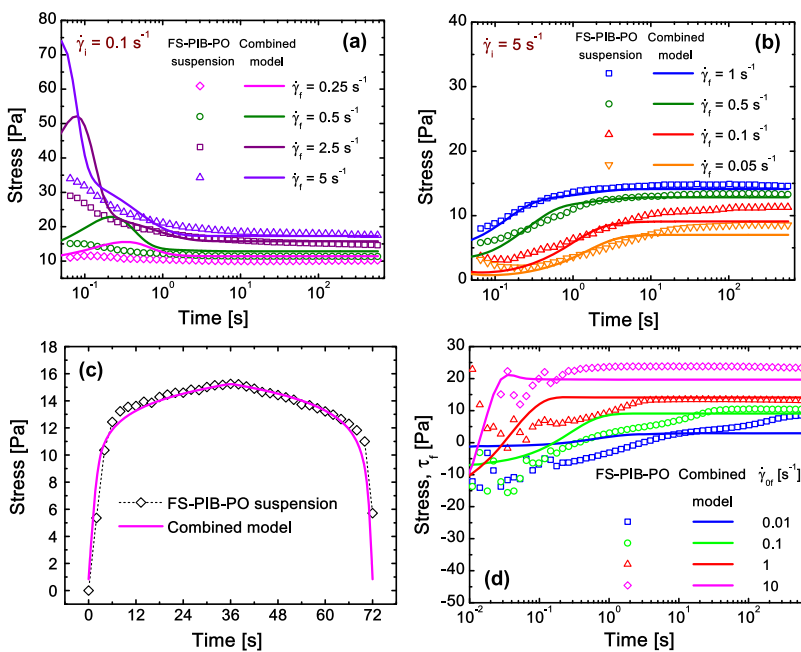


FIG. 7. Data of (a) step up in shear rate from 0.1 s⁻¹ to four different values and (b) step down in shear rate from 5 s⁻¹ to four other different values as indicated. Output stress profile from (c) the triangular ramp transient shear rate test and (d) flow reversal test at four different shear rates as indicated for the FS-PIB-PO suspension. Points represent experimental data, while the continuous lines represent the combined model fit discussed in Sec. III D.

A Giesekus model of the form represented in Eqs. (2d) and (2e) is used in this work. In the case of FS-PIB-PO suspension, the PIB-PO suspending medium acts as solvent, while the percolated flocs and entangled PIB polymer chains act as networks.

The best-case Giesekus model predictions of FS-PIB-PO suspension were obtained by optimizing over SAOS, steady shear, and step shear response data. The Giesekus model exhibits a crossover from viscoelastic liquid-like ($G' < G''$) to solid-like ($G' > G''$) followed by a slight rise in G'' post crossover indicating an increased dissipation at higher frequencies (refer to Fig. S5 and Table S3 of the supplementary material). However, this trend is very different from the dominant viscoelastic solid-like response of FS-PIB-PO suspension [Fig. 5(b)]. The KK analysis of the Giesekus model, shown in Fig. 8(a), indicates that the residuals are zero and the data are KK compliant. This indicates that the response is linear, causal, and time independent at low strain amplitudes, unlike the case for the FS-PIB-PO suspension (discussed earlier in Sec. III A). Furthermore, the Giesekus model predicts higher values of steady state stress and stronger shear thinning than those of the FS-PIB-PO suspension (Fig. S5c). All these results suggest that the Giesekus model needs further modification to capture in its entirety, the TEVP behavior of the suspension.

A viscoelastic solid-like model that incorporates yielding and time variant structural processes, such as the simple scalar thixotropic (SST) model,²¹ can also be utilized to evaluate the response of FS-PIB-PO suspension. The SST model has a phenomenological structure kinetics equation given by

$$\frac{d\beta}{dt} = k_{Brown}[-t_{r1}\beta|\dot{\gamma}| + (1 - \beta)] \quad (6)$$

and a Bingham-like base equation with an additional structural viscosity term, η_{ST} , given by

$$\tau = \tau_y + \eta\dot{\gamma} + \eta_\infty\dot{\gamma}, \quad (7a)$$

$$\tau_y = \beta\tau_{y0}, \quad \eta = \beta\eta_{ST}, \quad (7b)$$

where τ is the shear stress, $\dot{\gamma}$ is the shear rate, τ_{y0} is the constant yield stress, and η_∞ is the infinite shear viscosity. $t_{r1} = (k_{Break}/k_{Brown})^{-1}$ as the characteristic time for shear induced structure breakdown and $(k_{Brown})^{-1}$ as the characteristic time for structure recovery at rest, assisted by Brownian motion. It is important to note that the yield stress and viscosity contributions in the model are allowed to vary with the current structural level, β [Eq. (7b)].

To closely mimic the experiments, the models are simulated assuming that the initial state is either fully broken (i.e., $\beta_0 = 0$) or fully structured (i.e., $\beta_0 = 1$).

The SST model exhibits $G' > G''$ with G' being constant and G'' following an approximate linear increase with frequency (refer to Fig. S5 and Table S3 of the supplementary material). A slight decrease is also observed in both the moduli at high frequencies (Fig. S5a). However, this trend is very different from the SAOS response of FS-PIB-PO suspension [Fig. 5(b)]. The value of $\beta_{average} (= [\max(\beta_{wave}) + \min(\beta_{wave})]/2)$ indicates the level of structure at the steady terminal oscillation state corresponding to each frequency. The model results show that although the structure completely builds up at low/intermediate frequencies (i.e., $\beta_{average} = 1$), the buildup is only partial corresponding to $\beta_{average} = 0.62$ at higher frequencies (Fig. S5b). $\beta_{amplitude} (= [\max(\beta_{wave}) - \min(\beta_{wave})]/2)$ also indicates that β_{wave} values are low ($\sim 10^{-4}$) and its non-monotonic trend with frequency is contributed by the corresponding structural events. This clearly indicates the inherent time dependence of SST model. This could be the reason for higher magnitudes of KK residuals of the corresponding moduli as shown in Fig. 8(a). Furthermore, these residuals exhibit a definitive trend confirming that the data are not KK compliant, similar to that of FS-PIB-PO suspension (discussed earlier in Sec. III A). Although the SST model describes the steady shear response of FS-PIB-PO suspension very well (Fig. S5c), it does not predict the SAOS response even qualitatively. Thus, the SST model is also insufficient to predict in its entirety, the TEVP behavior of the suspension.

A popular strategy to improve viscoelastic fluid-like models involves inclusion of additional terms/equations to capture the time dependent structural processes.^{8,35,36} In this work, we attempt incorporation of structure kinetics [Eq. (6)] in the Giesekus model [Eq. (2)] by describing appropriately chosen model parameters as functions of the structure factor given by

$$\lambda_1 = \lambda_{10}\beta, \quad (8a)$$

$$\eta_p = \eta_{p0}\beta, \quad (8b)$$

where λ_{10} and η_{p0} are model parameters representing the characteristic relaxation time and polymer viscosity, respectively, at the initial structural state. The solvent viscosity is assumed to remain unaffected by structure kinetics. The SAOS response of the modified Giesekus model is qualitatively similar to that of a pure Giesekus model (refer to Fig. S6 and Table S3 of the supplementary material). However, with the increase in t_{r1} , the G'' curve shifts toward the G'

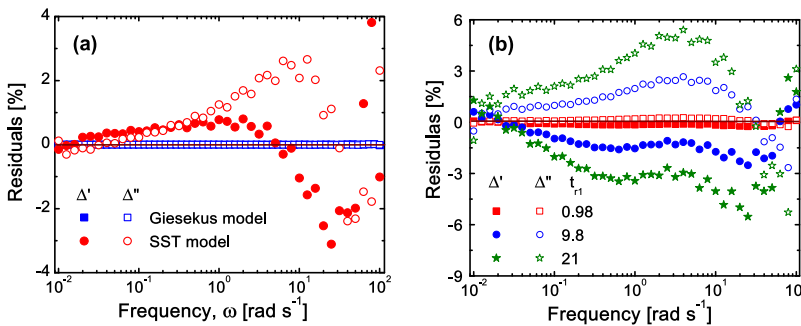


FIG. 8. Residuals from the KK analysis of models, evaluated for the SAOS response of FS-PIB-PO suspension at a strain amplitude of 1% (shown in Figs. S5 and S6 of the supplementary material), computed using Eq. (5). (a) Best fit Giesekus and SST models. (b) Giesekus with structure kinetics model at varying t_{r1} of 0.98 s, 9.8 s, and 21 s.

curve at intermediate/high frequencies indicating an increased dissipation (Fig. S6a). Such features are attributed to intrinsic structural changes such as an increase in the extent of structure breakdown due to an increase in k_{Break} with an increase in t_{r1} . This is manifested as an increase in the decay of $\beta_{average}$ with frequency, i.e., it goes from 1 (fully built up) to 0.62, 0.14, and 0.07 (partially built up) at t_{r1} values of 0.98 s, 9.8 s, and 21 s, respectively (Fig. S6b). Correspondingly, there is a difference in the non-monotonic trend of $\beta_{amplitude}$ with frequency at different t_{r1} , although the values are low. All these clearly indicate the inherent time dependence of the model. This could be the reason for the increase in KK residuals, $|\Delta'|$ and $|\Delta''|$, with an increase in t_{r1} , as shown in Fig. 8(b). The definitive trend of residuals vs frequency also becomes more apparent, leading to a decrease in the KK compliance with an increase in t_{r1} . Likewise, although the steady shear response of this model is qualitatively similar to that of pure Giesekus, the steady state stress values are greatly lowered in the case of former than the latter, with an increase in t_{r1} (Fig. S6c). We note that the Giesekus with structure kinetics model, with $t_{r1} = 21$ s, gives better predictions of the SAOS (especially at higher frequencies) and steady shear response than that of pure Giesekus. However, the overall response of this model under SAOS is still very different from that of the FS-PIB-PO suspension. This indicates that the

Giesekus with structure kinetics model is also inadequate to describe in its entirety, the TEVP behavior of the suspension.

Other models based on theories/approaches either similar to or different from that of Giesekus and SST models were also evaluated to match the SAOS, steady shear, and step shear response of FS-PIB-PO suspension (refer to Figs. S7–S10 and Tables S2 and S3 of the supplementary material). Inferences from their response predictions for different protocols are summarized in Table II. The conclusions from the KK analysis of their SAOS data are briefed in Table III (also refer to Table S5 of the supplementary material). Since they provided an unsatisfactory description of the TEVP behavior, these models are not investigated further. Based on the insights, we propose that a combined model is essential to describe a majority of the TEVP behavior features. The combined model must include strong viscoelastic contributions, yielding, and multiple thixotropic time scales. Therefore, a combination of SST [Eqs. (6) and (7)] and Giesekus with structure kinetics model [Eqs. (2), (6) and (8)] is formulated such that each of them follows the same structure kinetics equation, but different structure breakdown and buildup time scales. The overall set of equations of the combined model are summarized in Table I. The subscript “G” in Table I refers to quantities of the Giesekus with structure kinetics submodel of the combined

TABLE II. Summary of the models evaluated to describe the response of the FS-PIB-PO suspension for rheological tests. The poor, moderate, and good match of model predictions with experimental results are designated as “*,” “**,” and “***,” respectively (based on the criteria discussed in Sec. II D).

Model	Steady shear	Step shear	SAOS
Maxwell [Eq. (1), Table S2, and Fig. S7]	*	*	*
Standard linear solid (SLS) [Eq. (2), Table S2, and Fig. S7]	*	*	**
Giesekus [Eq. (2), Fig. 8, and Fig. S5]	*	*	*
Weak gel [Eq. (3), Table S2, and Fig. S8]	*	*	***
Modified weak gel [Eq. (4), Table S2, and Fig. S8]	*	*	***
Combined weak gel–Giesekus [Eq. (5), Table S2, and Fig. S9]	*	*	***
Modified combined weak gel–Giesekus [Eq. (6), Table S2, and Fig. S9]	*	*	***
Elastoviscoplastic (EVP) [Eq. (7), Table S2, and Fig. S10]	*	*	*
Simple scalar thixotropic (SST) [Eqs. (6) and (7), Fig. 8, and Fig. S5]	***	***	*
Giesekus with structure kinetics [Eqs. (2), (6) and (8), Fig. 8, and Fig. S6]	**	*	**
Giesekus with structure kinetics + SST (Table I, Figs. 7 and 9–12)	***	***	***

TABLE III. Summary of experimental systems/models subjected to KK analysis of their SAOS response. It is recommended that residuals <1% imply good KK compliance (+) and >1% imply otherwise (–).

Material/model	KK compliance	Criteria violated
Silicone oils, PIB-PO blend (Table S1)	+	None
FS-PO, FS-PIB-PO suspensions (Table S1)	–	Time independence
Maxwell, SLS, Giesekus, weak gel, combined weak gel–Giesekus, and EVP models (at low γ_0 values) [Eq. (2) and Tables S2 and S5]	+	None
Modified weak gel model (Tables S2 and S5)	–	Linearity
Modified combined weak gel–Giesekus model (Tables S2 and S5)	–	Linearity
Simple scalar thixotropic (SST) model [Eqs. (6) and (7) and Table S5]	–	Time independence
Giesekus with structure kinetics model [Eqs. (2), (6), and (8) and Table S5]	–	Time independence
Giesekus with structure kinetics + SST model (Tables I and S5)	–	Time independence

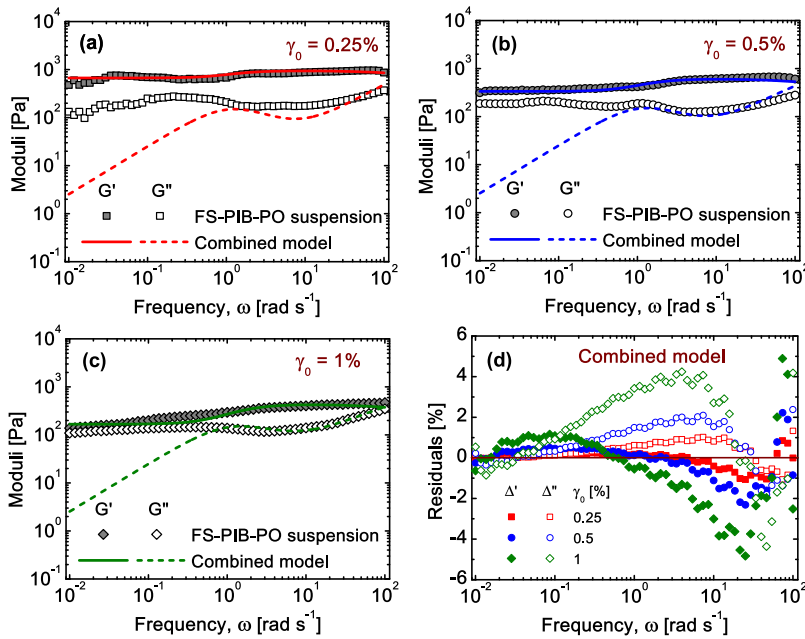


FIG. 9. The SAOS response of best fit combined Giesekus with structure kinetics and SST model for the FS-PIB-PO suspension at a strain amplitude of (a) 0.25%, (b) 0.5%, and (c) 1%. Points represent experimental data, while the continuous lines represent model fits. (d) Residuals from the KK analysis of model data shown in (a), (b), and (c) computed using Eq. (5).

model. Similarly, the subscript “S” refers to quantities of the SST submodel of the combined model. The 12 combined model parameters are $\eta_s, \eta_{p0}, \lambda_{10}, \alpha, k_{Brown-G}, t_{r1-G}, \eta_\infty, \eta_{ST}, \tau_{y0}, k_{Brown-S}, t_{r1-S},$ and W_G .

The best fit parameters of the combined model for FS-PIB-PO suspension are listed in Table S4 of the supplementary material. It can be seen from Figs. 9(a)–9(c) that the combined model describes the SAOS response semi-quantitatively at strain amplitudes (γ_0) of 0.25%, 0.5% and 1%, respectively (with the exception of G'' at low frequencies). It perfectly captures the significant features such as the predominant viscoelastic solid-like behavior and the corresponding trends of G' and G'' with frequency. KK analysis of the model SAOS response reveals an increase in the residuals, $|\Delta'|$ and $|\Delta''|$, with an increase in γ_0 , indicating poorer KK compliance as shown in Fig. 9(d). The values of $\beta_{average}$ and $\beta_{amplitude}$, as predicted by the combined model, are plotted as a function of frequency in Fig. 10. Contributions from the Giesekus with structure kinetics submodel

and the SST submodel of the combined model are presented in Figs. 10(a) and 10(b), respectively. It is seen that with an increase in γ_0 , there is an increase in the decay of $\beta_{average}$ with frequency for both the submodels of the combined model. Correspondingly, there is also a difference in the non-monotonic trend of $\beta_{amplitude}$ with frequency for both the submodels of the combined model at different γ_0 , although the values are low. These results can be attributed to the stronger structural changes induced by increasing γ_0 . We note that quantitative prediction of the SAOS response is good, especially at higher frequencies, wherein thixotropic structure break-down time scales are predominant (i.e., $\beta_{average}$ and $\beta_{amplitude}$ values for both the submodels of the combined model decrease at higher frequencies).

The steady state flow curve prediction of the combined model, along with the experimental data, is presented in Fig. 11(a), and there is a good agreement between the experimental and the model steady state stresses. The β values of Giesekus with

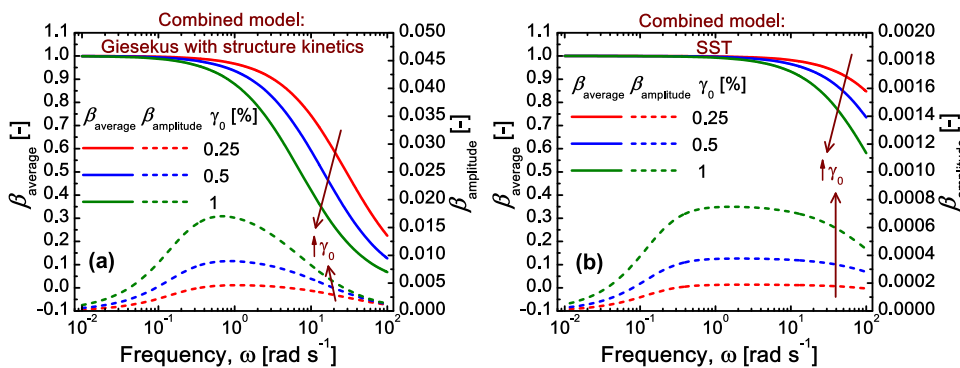


FIG. 10. Response of the best fit combined model for FS-PIB-PO suspension. Structure factor (average and amplitude values) for (a) Giesekus with structure kinetics submodel and (b) SST submodel corresponding to the SAOS data of model shown in Fig. 9.

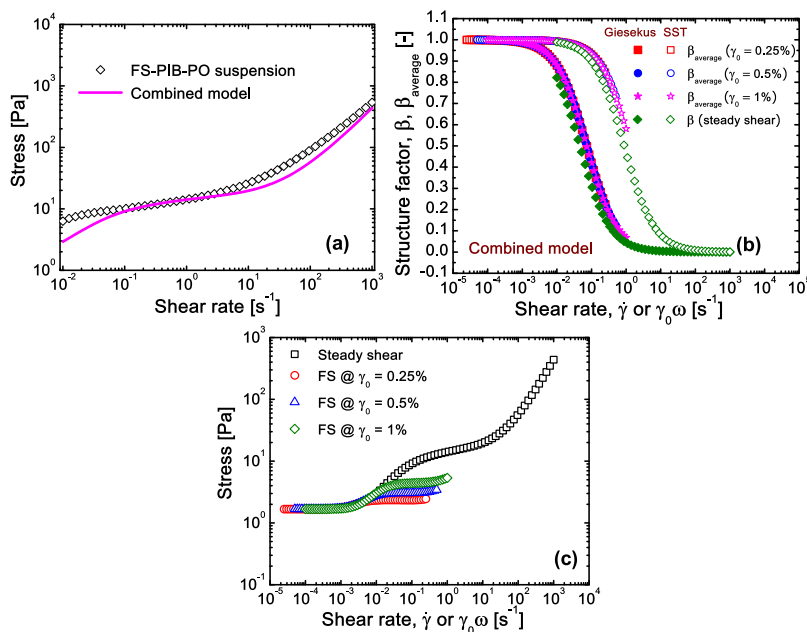


FIG. 11. Response of the best fit combined model for FS-PIB-PO suspension. (a) Steady state flow curves. (b) Structure factor, β (during steady shear) and $\beta_{average}$ (during SAOS), of the Giesekus with structure kinetics submodel and SST submodel of the combined model as a function of shear rate. (c) Stress as a function of shear rate during steady shear and frequency sweep (at strain amplitudes of 0.25%, 0.5%, and 1%) of the combined model.

structure kinetics submodel and SST submodel of the combined model during steady shear, as a function of shear rate, are shown in Fig. 11(b). The $\beta_{average}$ values of Giesekus with structure kinetics submodel and SST submodel of the combined model during SAOS, obtained from Figs. 10(a) and 10(b), respectively, are also plotted against the corresponding shear rates ($\dot{\gamma}_0 = \gamma_0\omega$) in Fig. 11(b). It can be clearly seen that for both the submodels, the values of $\beta_{average}$ at different strain amplitudes (during SAOS) and β (during steady shear) appear to superimpose, indicating that the processes occurring during both the tests are similar. The quantitative difference between the $\beta_{average}/\beta$ values of the Giesekus with structure kinetics submodel and the SST submodel of the combined model ($\sim 10^{-2} - 10^1$ s⁻¹) indicates the difference in their contributions to the response at different shear rates (during the different tests). The Giesekus with structure kinetics submodel shows a stronger structure breakdown at lower shear rates itself (usually probed during SAOS), while the SST submodel shows a stronger structure breakdown only at higher shear rates (usually probed during steady shear). Hence, it can be postulated that the flocculated network structure of FS-PIB-PO suspension exhibits dominant viscoelasticity and thixotropy with less apparent yielding during SAOS ($\sim 10^{-5} - 10^0$ s⁻¹). During steady shear, the yielding and thixotropic processes are prevalent with less apparent viscoelasticity ($\sim 10^{-2} - 10^3$ s⁻¹). Figure 11(c) presents the stresses during SAOS, plotted against the corresponding shear rates ($\dot{\gamma}_0 = \gamma_0\omega$), and the steady shear stresses of the combined model. It can be clearly seen that they do not perfectly superpose. This was observed earlier even for the experimental results [Fig. 6(b)]. Since the combined model effectively describes the entire flow curve, it can be concluded that structural kinetics with different types of base models is essential to describe the TEVP behavior of the suspension.

The stress waveforms obtained at three different low strain amplitudes of 0.25%, 0.5%, and 1% from the amplitude sweeps of FS-PIB-PO suspension [Fig. 5(a)] are presented in Fig. 12. It is seen that the experimental elastic [Fig. 12(a)] and viscous [Fig. 12(b)] Lissajous curves are elliptical with the phase angle, $0 < \delta \ll \pi/2$, indicating a viscoelastic solid-like response. There is no significant change in the dissipation (i.e., area of the Lissajous curves) with respect to either the strain amplitudes or frequencies probed. The combined model (computed at the optimized parameter set) yields good predictions of the cycle response, especially at a high frequency of 10 rad s⁻¹. The poor agreement of experimental and model cycle stresses at a low frequency of 1 rad s⁻¹ can be attributed to the under-prediction of G'' at low frequencies in the corresponding SAOS as shown in Figs. 9(a)–9(c), respectively.

The combined model also provides good, semi-quantitative, description of the step up and step down shear response as shown in Figs. 7(a) and 7(b), respectively. Viscoelastic rise in the step up shear response is followed by the subsequent thixotropic decay; in addition, all features of the step down shear response are well captured. As mentioned earlier in Sec. II D, since the best fit combined model parameters are obtained by optimizing over steady shear, step shear, and SAOS, the predictions for other transient shear protocols, which were not utilized in the optimization process, are simulated and presented. The combined model predictions for triangular ramp tests, obtained for FS-PIB-PO suspension, also matched well with the corresponding experimental stresses as shown in Fig. 7(c). In the case of flow reversal tests, although the combined model predictions indicate an initial viscoelastic stress increase at all the shear rates investigated as shown in Fig. 7(d), the second stress increase especially observed at low shear rates is totally absent. Therefore, the combined model fails to describe the two-step relaxation during flow reversal even qualitatively. In order

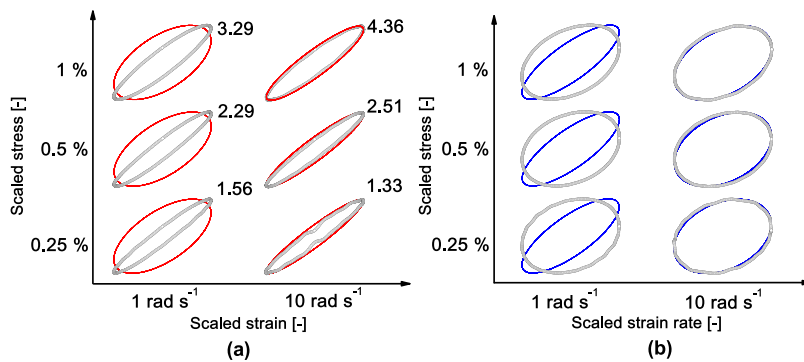


FIG. 12. The Pipkin space of FS-PIB-PO suspension at strain amplitudes of 0.25%, 0.5%, and 1% with (a) elastic Lissajous curves and (b) viscous Lissajous curves. Points represent experimental data, while the continuous lines represent combined model fit. The stress amplitude is mentioned on the top right corner of each subplot in (a).

to specifically capture such features of the flow reversal tests, models equipped with terms that define shear direction dependent plasticity are essential.^{9,10} Often, such modifications can greatly complicate modeling aspects and, therefore, are out of scope of this work. It should be noted that such plasticity based modeling does not capture the dominant viscoelastic and thixotropic phenomena during SAOS.¹⁰

Table II presents the list of models evaluated in this work and their effectiveness in fitting the steady shear, step shear, and SAOS responses. Among the models evaluated, the proposed combined model effectively captures all the major features of the complex TEVP behavior exhibited by the FS-PIB-PO suspension. Table III gives a concise account of experimental systems and models with KK compliance of their SAOS response and possible reasons for the deviation whenever observed (also refer to Tables S1 and S5 of the supplementary material).

IV. CONCLUSIONS

In this work, we explored the small amplitude oscillatory shear (SAOS) response of a model thixotropic elastoviscoplastic (TEVP) suspension of fumed silica in polyisobutylene/paraffin oil (FS-PIB-PO) to understand the contributions from the suspending medium and polymer/particle nature of the material. Violations of linearity, causality, and/or time independence criteria can be identified by Kramers–Kronig (KK) validation of the SAOS data. We recommend that apart from steady shear and transient shear (i.e., step shear, triangular ramp, and flow reversal) techniques, SAOS analysis should also be performed to obtain a better understanding of the material structures and their influence on its rheological properties.

Models that capture the response from steady shear and step up/step down shear do not adequately describe the SAOS response of the FS-PIB-PO suspension. A novel combination of the simple scalar thixotropic (SST) and the Giesekus with structure kinetics model is shown to describe the results of the suite of tests (SAOS, steady and step shear) for the suspension semi-quantitatively. Furthermore, the model also gives good predictions for other transient tests (triangular ramp and flow reversal). This indicates that the suspension has at least two types of interleaving structures, one which breaks down at a lower shear rate and has a viscoelastic like behavior and another which breaks down at a higher shear rate and has a solid like behavior. Thus, the hitherto known structural mechanisms underlying the TEVP behavior, i.e., viscoelastic, yielding, and multiple thixotropic

relaxation processes, are well captured. The residuals in KK transform of SAOS data are found to be sensitive to small changes in strain amplitude or structure dependent model parameters. In summary, we demonstrate the utility of applying a combination of rheological protocols including SAOS and KK analysis (for SAOS data validation) to understand thixotropy in complex TEVP systems.

SUPPLEMENTARY MATERIAL

See the supplementary material for additional details related to SAOS/KK analysis of experimental systems and phenomenological models, model parameters, and comparison of steady shear with LAOS response.

ACKNOWLEDGMENTS

The authors acknowledge Dr. B. A. Boukamp, Faculty of Science and Technology, University of Twente, The Netherlands, for providing the free “Linear KKT” software.

REFERENCES

- C. Huang, N. Siskovic, R. Robertson, W. Fabisiak, E. H. Smitherberg, and A. L. Copley, “Quantitative characterization of thixotropy of whole human blood,” *Biorheology* **12**, 279–282 (1975).
- C. H. Lee, V. Moturi, and Y. Lee, “Thixotropic property in pharmaceutical formulations,” *J. Controlled Release* **136**, 88–98 (2009).
- S. M. Razavi and H. Karazhiyan, “Flow properties and thixotropy of selected hydrocolloids: Experimental and modeling studies,” *Food Hydrocolloids* **23**, 908–912 (2009).
- C. Van Der Geest, V. C. B. Guersoni, D. Merino-Garcia, and A. C. Bannwart, “A modified elasto-viscoplastic thixotropic model for two commercial gelled waxy crude oils,” *Rheol. Acta* **54**, 545–561 (2015).
- C. F. Goodeve and G. W. Whitfield, “The measurement of thixotropy in absolute units,” *Trans. Faraday Soc.* **34**, 511–520 (1938).
- J. Mewis, “Thixotropy—A general review,” *J. Non-Newtonian Fluid Mech.* **6**, 1–20 (1979).
- H. A. Barnes, “Thixotropy—A review,” *J. Non-Newtonian Fluid Mech.* **70**, 1–33 (1997).
- J. Mewis and N. J. Wagner, “Thixotropy,” *Adv. Colloid Interface Sci.* **147–148**, 214–227 (2009).
- R. G. Larson and Y. Wei, “A review of thixotropy and its rheological modeling,” *J. Rheol.* **63**, 477–501 (2019).
- Y. Wei, M. J. Solomon, and R. G. Larson, “A multimode structural kinetics constitutive equation for the transient rheology of thixotropic elasto-viscoplastic fluids,” *J. Rheol.* **62**, 321–342 (2018).

- ¹¹D. Xie, G. G. Qiao, and D. E. Dunstan, "Flow-induced aggregation of colloidal particles in viscoelastic fluids," *Phys. Rev. E* **94**, 022610 (2016).
- ¹²D. Quemada, "Rheological modelling of complex fluids: II. shear thickening behavior due to shear induced flocculation," *Eur. Phys. J.: Appl. Phys.* **2**, 175–181 (1998).
- ¹³D. Quemada, "Rheological modelling of complex fluids: IV: Thixotropic and "thixoelastic" behaviour. start-up and stress relaxation, creep tests and hysteresis cycles," *Eur. Phys. J.: Appl. Phys.* **5**, 191–207 (1999).
- ¹⁴J. Vermant and M. J. Solomon, "Flow-induced structure in colloidal suspensions," *J. Phys.: Condens. Matter* **17**, R187–R216 (2005).
- ¹⁵K. Masschaele, J. Franssaer, and J. Vermant, "Flow-induced structure in colloidal gels: Direct visualization of model 2D suspensions," *Soft Matter* **7**, 7717–7726 (2011).
- ¹⁶P. R. de Souza Mendes and R. L. Thompson, "A critical overview of elasto-viscoplastic thixotropic modeling," *J. Non-Newtonian Fluid Mech.* **187–188**, 8–15 (2012).
- ¹⁷R. Radhakrishnan, T. Divoux, S. Manneville, and S. M. Fielding, "Understanding rheological hysteresis in soft glassy materials," *Soft Matter* **13**, 1834–1852 (2017).
- ¹⁸R. H. Ewoldt and G. H. McKinley, "Mapping thixo-elasto-visco-plastic behavior," *Rheol. Acta* **56**, 195–210 (2017).
- ¹⁹Y. M. Joshi and G. Petekidis, "Yield stress fluids and ageing," *Rheol. Acta* **57**, 521–549 (2018).
- ²⁰K. Dullaert and J. Mewis, "Thixotropy: Build-up and breakdown curves during flow," *J. Rheol.* **49**, 1213–1230 (2005).
- ²¹M. J. Armstrong, A. N. Beris, S. A. Rogers, and N. J. Wagner, "Dynamic shear rheology of a thixotropic suspension: Comparison of an improved structure-based model with large amplitude oscillatory shear experiments," *J. Rheol.* **60**, 433–450 (2016).
- ²²Y. Wei, M. J. Solomon, and R. G. Larson, "Quantitative nonlinear thixotropic model with stretched exponential response in transient shear flows," *J. Rheol.* **60**, 1301–1315 (2016).
- ²³J. S. Horner, M. J. Armstrong, N. J. Wagner, and A. N. Beris, "Investigation of blood rheology under steady and unidirectional large amplitude oscillatory shear," *J. Rheol.* **62**, 577–591 (2018).
- ²⁴M. Armstrong, J. Horner, M. Clark, M. Deegan, T. Hill, C. Keith, and L. Mooradian, "Evaluating rheological models for human blood using steady state, transient, and oscillatory shear predictions," *Rheol. Acta* **57**, 705–728 (2018).
- ²⁵H. T. Huynh, N. Roussel, and P. Coussot, "Aging and free surface flow of a thixotropic fluid," *Phys. Fluids* **17**, 033101 (2005).
- ²⁶S. Jabbari-Farouji, M. Atakhorrami, D. Mizuno, E. Eiser, G. H. Wegdam, C. MacKintosh, D. Bonn, and C. F. Schmidt, "High-bandwidth viscoelastic properties of aging colloidal glasses and gels," *Phys. Rev. E* **78**, 061402 (2008).
- ²⁷M. Agarwal and Y. M. Joshi, "Signatures of physical aging and thixotropy in aqueous dispersion of carbopol," *Phys. Fluids* **31**, 063107 (2019).
- ²⁸A. R. Jacob, E. Moghimi, and G. Petekidis, "Rheological signatures of aging in hard sphere colloidal glasses," *Phys. Fluids* **31**, 087103 (2019).
- ²⁹K. Dullaert and J. Mewis, "A structural kinetics model for thixotropy," *J. Non-Newtonian Fluid Mech.* **139**, 21–30 (2006).
- ³⁰B. C. Blackwell and R. H. Ewoldt, "A simple thixotropic–viscoelastic constitutive model produces unique signatures in large-amplitude oscillatory shear (LAOS)," *J. Non-Newtonian Fluid Mech.* **208–209**, 27–41 (2014).
- ³¹A. J. Apostolidis, M. J. Armstrong, and A. N. Beris, "Modeling of human blood rheology in transient shear flows," *J. Rheol.* **59**, 275–298 (2015).
- ³²M. J. Armstrong, A. N. Beris, S. A. Rogers, and N. J. Wagner, "Dynamic shear rheology and structure kinetics modeling of a thixotropic carbon black suspension," *Rheol. Acta* **56**, 811–824 (2017).
- ³³C. Brée, A. Demircan, and G. Steinmeyer, "Kramers-Kronig relations and high-order nonlinear susceptibilities," *Phys. Rev. A* **85**, 033806 (2012).
- ³⁴C. Bédard and A. Destexhe, "Generalized theory for current-source-density analysis in brain tissue," *Phys. Rev. E* **84**, 041909 (2011).
- ³⁵A. Mujumdar, A. N. Beris, and A. B. Metzner, "Transient phenomena in thixotropic systems," *J. Non-Newtonian Fluid Mech.* **102**, 157–178 (2002).
- ³⁶R. G. Larson, "Constitutive equations for thixotropic fluids," *J. Rheol.* **59**, 595–611 (2015).
- ³⁷A. Beris, E. Stiakakis, and D. Vlassopoulos, "A thermodynamically consistent model for the thixotropic behavior of concentrated star polymer suspensions," *J. Non-Newtonian Fluid Mech.* **152**, 76–85 (2008).
- ³⁸J. Labanda, P. Marco, and J. Llorens, "Rheological model to predict the thixotropic behaviour of colloidal dispersions," *Colloids Surf., A* **249**, 123–126 (2004).
- ³⁹J. Labanda and J. Llorens, "A structural model for thixotropy of colloidal dispersions," *Rheol. Acta* **45**, 305–314 (2006).
- ⁴⁰H. P. A. de Deus, C. O. Negrão, and A. T. Franco, "The modified Jeffreys model approach for elasto-viscoplastic thixotropic substances," *Phys. Lett. A* **380**, 585–595 (2016).
- ⁴¹R. B. Bird, R. C. Armstrong, and O. Hassager, *Dynamics of Polymeric Liquids*, Fluid Mechanics Vol. 1 (John Wiley & Sons, New York, 1987).
- ⁴²S. A. Rogers, P. T. Callaghan, G. Petekidis, and D. Vlassopoulos, "Time-dependent rheology of colloidal star glasses," *J. Rheol.* **54**, 133–158 (2010).
- ⁴³P. M. Mwasame, A. N. Beris, R. B. Diemer, and N. J. Wagner, "A constitutive equation for thixotropic suspensions with yield stress by coarse-graining a population balance model," *AIChE J.* **63**, 517–531 (2017).
- ⁴⁴P. R. de Souza Mendes, K. R. Rajagopal, and R. L. Thompson, "A thermodynamic framework to model thixotropic materials," *Int. J. Non-Linear Mech.* **55**, 48–54 (2013).
- ⁴⁵S. Varchanis, G. Makrigiorgos, P. Moschopoulos, Y. Dimakopoulos, and J. Tsamopoulos, "Modeling the rheology of thixotropic elasto-visco-plastic materials," *J. Rheol.* **63**, 609–639 (2019).
- ⁴⁶J. S. Horner, M. J. Armstrong, N. J. Wagner, and A. N. Beris, "Measurements of human blood viscoelasticity and thixotropy under steady and transient shear and constitutive modeling thereof," *J. Rheol.* **63**, 799–813 (2019).
- ⁴⁷K. Dullaert and J. Mewis, "A model system for thixotropy studies," *Rheol. Acta* **45**, 23–32 (2005).
- ⁴⁸M. Urquidi-Macdonald, S. Real, and D. D. Macdonald, "Applications of Kramers–Kronig transforms in the analysis of electrochemical impedance data—III. stability and linearity," *Electrochim. Acta* **35**, 1559–1566 (1990).
- ⁴⁹H. C. Booij and G. P. J. M. Thoone, "Generalization of Kramers-Kronig transforms and some approximations of relations between viscoelastic quantities," *Rheol. Acta* **21**, 15–24 (1982).
- ⁵⁰L. Rouleau, J.-F. Deü, A. Legay, and F. L. Lay, "Application of Kramers–Kronig relations to time–temperature superposition for viscoelastic materials," *Mech. Mater.* **65**, 66–75 (2013).
- ⁵¹N. Makris and G. Kampas, "Analyticity and causality of the three-parameter rheological models," *Rheol. Acta* **48**, 815–825 (2009).
- ⁵²H. H. Winter, "Analysis of dynamic mechanical data: Inversion into a relaxation time spectrum and consistency check," *J. Non-Newtonian Fluid Mech.* **68**, 225–239 (1997).
- ⁵³B. M. Erwin, S. A. Rogers, M. Cloitre, and D. Vlassopoulos, "Examining the validity of strain-rate frequency superposition when measuring the linear viscoelastic properties of soft materials," *J. Rheol.* **54**, 187–195 (2010).
- ⁵⁴J. K. G. Dhont and N. J. Wagner, "Superposition rheology," *Phys. Rev. E* **63**, 021406 (2001).
- ⁵⁵T. Pritz, "Unbounded complex modulus of viscoelastic materials and the Kramers–Kronig relations," *J. Sound Vib.* **279**, 687–697 (2005).
- ⁵⁶B. A. Boukamp, "A linear Kronig-Kramers transform test for admittance data validation," *J. Electrochem. Soc.* **142**, 1885–1894 (1995).
- ⁵⁷B. A. Boukamp, "Electrochemical impedance spectroscopy in solid state ionics: Recent advances," *Solid State Ionics* **169**, 65–73 (2004).
- ⁵⁸M. Mours and H. H. Winter, "Time-resolved rheometry," *Rheol. Acta* **33**, 385–397 (1994).
- ⁵⁹H. Barthel, "Surface interactions of dimethylsiloxy group-modified fumed silica," *Colloids Surf., A* **101**, 217–226 (1995).
- ⁶⁰S. R. Raghavan, H. J. Walls, and S. A. Khan, "Rheology of silica dispersions in organic liquids: New evidence for solvation forces dictated by hydrogen bonding," *Langmuir* **16**, 7920–7930 (2000).
- ⁶¹C. Frederick and P. Armstrong, "A mathematical representation of the multiaxial Bauschinger effect," *Mater. High Temp.* **24**, 1–26 (2007).

⁶²A. Kate Gurnon and N. J. Wagner, “Large amplitude oscillatory shear (LAOS) measurements to obtain constitutive equation model parameters: Giesekus model of banding and nonbanding wormlike micelles,” *J. Rheol.* **56**, 333–351 (2012).

⁶³K. A. Ramya, R. Srinivasan, and A. P. Deshpande, “Nonlinear measures and modeling to examine the role of physical and chemical crosslinking in poly(vinyl alcohol)-based crosslinked systems,” *Rheol. Acta* **57**, 181–195 (2018).